Multiphoton-assisted absorption of terahertz radiation in InAs/AlSb heterojunctions

J. C. Cao
State Key Laboratory of Functional Materials for Informatics, Shanghai Institute of Microsystem and Information Technology, Chinese Academy of Sciences, 865 Changning Road, Shanghai 200050, People's Republic of China

X. L. Lei
Department of Physics, Shanghai Jiaotong University, 1954 Huashan Road, Shanghai, 200030, People's Republic of China and Shanghai Institute of Microsystem and Information Technology, Chinese Academy of Sciences, 865 Changning Road, Shanghai 200050, People's Republic of China

(Received 9 August 2002; revised manuscript received 29 October 2002; published 7 February 2003)

We have calculated the free-carrier absorption percentage of intense terahertz (THz) radiation in InAs/AlSb heterojunctions (HJ's), by considering multiple photon process and conduction-valence interband impact ionization within the extended balance-equation theory. In the calculations we have included the electron-acoustic-phonon scattering, electron-polar-optical-phonon scattering, and elastic scattering both from the remote charged impurities and from the background impurities, and as many as needed hole subbands and multiphoton channels are self-consistently taken into account for getting a required accuracy. It is indicated that the THz radiation with a larger amplitude E_{ac} or a lower frequency f_{ac} has a stronger effect on electric transport characteristics. Good agreement is obtained between the calculated absorption percentages and the available experimental data for InAs/AlSb HJ's at $f_{ac}=0.64$ THz.

DOI: 10.1103/PhysRevB.67.085309 PACS number(s): 78.20.Ci, 73.50.Fq, 73.50.Gr, 72.10.Bg

I. INTRODUCTION

Under the influence of terahertz (THz) radiation, low-dimensional electron gas exhibits many interesting phenomena,[1–5] such as THz radiation-induced dc current suppression,[1] multiphoton-assisted resonant tunneling,[2] negative absolute resistance,[3] and Shapiro steps on dc current-voltage curve.[4] A few years ago, Markelz and Asmar *et al.*[5] made far-infrared (THz) transmissions, reflections, and dc photoconductivity measurements to study free-carrier absorption and impact ionization caused by THz radiations in InAs/AlSb heterojunctions (HJ's). These experimental advances motivated new theoretical interests in THz optic electronics.[6–12] One of the authors recently developed a set of balance equations[6–8] for electron transport in semiconductors driven by an intense THz radiation field. In the balance-equation theory the slowly varying part of the center-of-mass velocity is distinguished from the rapid oscillating part of it, and all the multiphoton processes due to the intense THz radiation are included. The equations has been successfully used to study the effect of an intense THz radiation on electron transport in quasi-two-dimensional (2D) systems[6,7] and in superlattice minibands.[8] The purpose of this work is to extend the balance equation approach[6–8] to include impact ionization (II) process,[13,14] and apply it to study free-carrier absorption and electron-hole generation in InAs/AlSb HJ's driven by THz radiations having various frequency and strength. Multiple photon processes are investigated in detail. The free-carrier absorption percentages of intense terahertz (THz) radiation in InAs/AlSb HJ's are calculated by considering conduction-valence interband II, and quantitatively compared to the available experimental data.[5]

II. BALANCE EQUATIONS INCLUDING MULTIPHOTON EFFECT AND II PROCESS

We consider a semiconductor HJ with a 2D energy wave-vector relation $\varepsilon_{s,\mathbf{k}_\parallel}$, where s is the subband index and $\mathbf{k}_\parallel=(k_x,k_y)$ is the 2D wave vector. When a uniform dc (or slowly varying) electric field $\mathbf{E}_0$ and a uniform sinusoidal radiation field with the frequency f_{ac} and the amplitude $\mathbf{E}_{ac}$,

$$\mathbf{E}(t)=\mathbf{E}_0+\mathbf{E}_{ac}\sin(2\pi f_{ac}t), \tag{1}$$

are applied in the direction parallel to the HJ interface, the transport quantities will undergo both the rapid oscillation (due to high-frequency radiation field) and the slow variation (due to E_0 and intrinsic relaxation times of the system). If we measure all the quantities as the average over a time interval much longer than the period of the radiation field, the carrier conduction can be described by the following equations for the force, the energy, and the carrier number balance:[6]

$$\frac{d\mathbf{v}}{dt}=e\mathbf{E}_0\cdot\mathcal{K}+\mathbf{A}_{ei}+\mathbf{A}_{ep}+\mathbf{A}_{II}-g\mathbf{v}, \tag{2}$$

$$\frac{dh_e}{dt}=e\mathbf{E}_0\cdot\mathbf{v}-W_{ep}-W_{II}-gh_e+S_i+S_p+S_{II}, \tag{3}$$

$$\frac{dN}{dt}=gN. \tag{4}$$

The above equations are the direct extension of the recently developed balance equations[6] to include II process[13,14] in semiconductors driven by a THz electric field. The transport state of electrons is described by the effective momentum shift $\mathbf{p}_d$, electron temperature T_e, and electron chemical po-

tential μ determined by electron sheet density, $N=2\Sigma_{s,\mathbf{k}_\parallel} f[(\varepsilon_s\mathbf{k}_\parallel)-\mu)/T_e]$ with $f(x)=1/[\exp(x)+1]$ the Fermi distribution function. On the other hand, since the effective hole mass is usually much larger than that of the electron, the drift movement and heating of hole gas are not noticeable in comparison with those of the electron gas, thus the hole gas may be described by the lattice temperature T and hole chemical potential μ^h. In Eqs. (2)–(4), e is the carrier charge, g is the net electron-hole generation rate by balancing impact ionization generation and Auger recombination. $\mathbf{A}_{\rm ei}$, $\mathbf{A}_{\rm ep}$, and $\mathbf{A}_{\rm II}$ are the frictional accelerations respectively due to electron-impurity scattering, electron-phonon scattering, and conduction-valence interband II process. $W_{\rm ep}$ and $W_{\rm II}$ are the energy-loss rates respectively due to electron-phonon scattering and conduction-valence interband II process. Their explicit expressions can be found in Refs. 13–15. $S_{\rm i}$, $S_{\rm p}$, and $S_{\rm II}$ are the energy-gain rates of the electron system from the radiation field through the multiphoton process ($n=\pm1,\pm2,...$) in association with electron-impurity interaction, electron-phonon interaction, and II process, respectively. They are respectively expressed by

$$S_{\rm i}=\frac{1}{N}\sum_{s',s,\mathbf{q}_\parallel}|\tilde{U}_{s's}(\mathbf{q}_\parallel)|^2\sum_{n=-\infty}^{\infty}J_n^2(\mathbf{q}_\parallel\cdot\mathbf{r}_\omega)\times n\omega\Pi_2(s',s,\mathbf{q}_\parallel,\omega_0-n\omega), \tag{5}$$

$$S_{\rm p}=\frac{2}{N}\sum_{s',s,\mathbf{q},\lambda}|\tilde{M}_{s's}(\mathbf{q},\lambda)|^2\sum_{n=-\infty}^{\infty}J_n^2(\mathbf{q}_\parallel\cdot\mathbf{r}_\omega)\times n\omega\Pi_2(s',s,\mathbf{q}_\parallel,\Omega_{\mathbf{q}\lambda}+\omega_0-n\omega)\times\left[n\left(\frac{\Omega_{\mathbf{q}\lambda}}{T}\right)-n\left(\frac{\Omega_{\mathbf{q}\lambda}+\omega_0-n\omega}{T_e}\right)\right], \tag{6}$$

and

$$S_{\rm II}=\frac{2}{N}\sum_{s',s,\mathbf{k}_\parallel,\mathbf{q}_\parallel}|\tilde{M}^{\rm II^3}_{s',s}(\mathbf{q}_\parallel)|^2\sum_{n=-\infty}^{\infty}J_n^2(\mathbf{q}_\parallel\cdot\mathbf{r}_\omega)\times n\omega\Pi_2(s',s,\mathbf{q}_\parallel,\omega_2-n\omega)\times\left[f\left(\frac{\xi_{\mathbf{k}_\parallel-\mathbf{q}_\parallel}}{T_e}\right)+n\left(\frac{\omega_2-n\omega}{T_e}\right)\right]\times\left[f\left(\frac{\xi_{\mathbf{k}_\parallel}}{T}\right)-f\left(\frac{\omega_1+mv^2/2+\varepsilon_k^h+\mu}{T_e}\right)\right], \tag{7}$$

in which $\mathbf{r}_\omega=e\mathbf{E}_{\rm ac}/m\omega^2$, $\omega=2\pi f_{\rm ac}$ is the angular frequency, $\mathbf{q}=(\mathbf{q}_\parallel,q_z)$ is the three-dimensional phonon wave vector with $\mathbf{q}_\parallel=(q_x,q_y)$, $\omega_0=\mathbf{q}_\parallel\cdot\mathbf{v}$, $\omega_1=k_xv$, $\omega_2=\omega_1+mv^2/2+\varepsilon^h_{\mathbf{k}_\parallel}+\varepsilon_{s,\mathbf{k}_\parallel-\mathbf{q}_\parallel}$, $\xi_{\mathbf{k}_\parallel}=\varepsilon_{s,\mathbf{k}_\parallel}-\mu$, $\xi^h_{\mathbf{k}_\parallel}=\varepsilon^h_{\mathbf{k}_\parallel}-\mu^h$, $\varepsilon^h_{\mathbf{k}_\parallel}=E_g+\mathbf{k}_\parallel^2/(2m_h)$ is the hole dispersion with m_h the effective hole mass. Since the separations between different hole subbands are much smaller than those of electron subbands, more hole subbands would take part in the transport process than electron subbands do. For simplicity, we will neglect their separation but include contributions of a finite number of hole subbands, which are implicitly included in the summations of all the above expressions. In Eqs. (5)–(7) $n(x)=1/[\exp(x)-1]$ is the Bose function, and E_g is the band gap between the bottom of conduction band and the top of valence band. $\Pi_2(s',s,\mathbf{q}_\parallel,\Omega)$ is the imaginary part of electron-electron correlation functions, which shares the same expression with that given in Ref. 16. $J_n(x)$ is the nth-order Bessel function. $\tilde{U}_{s's}(\mathbf{q}_\parallel)$ and $\tilde{M}_{s's}(\mathbf{q},\lambda)$ are the matrix elements of electron-impurity interaction and electron-phonon interaction, respectively. $\Omega_{\mathbf{q}\lambda}$ is the phonon frequency of wave vector $\mathbf{q}$ and the branch index λ. $\tilde{M}^{\rm II}_{s',s}(\mathbf{q}_\parallel)$ is the Fourier representations of the band-band Coulomb interaction matrix element for II and Auger processes in 2D semiconductor system given by[16,17]

$$\tilde{M}^{\rm II}_{s',s}(\mathbf{q}_\parallel)=I_{s',s}(q_\parallel)I_{\rm cc}I_{\rm cv}\frac{e^2}{2\varepsilon_0\kappa q_\parallel\xi(q_\parallel,0)}\equiv C_{\rm II}\frac{e^2}{2\varepsilon_0\kappa q_\parallel\xi(q_\parallel,0)}, \tag{8}$$

where $I_{\rm cc}$ and $I_{\rm cv}$ are overlap integrals of conduction-conduction bands and conduction-valence bands, respectively. κ is the dielectric constant of semiconductor. $I_{s',s}(q_\parallel)$ is the form factor, and $\xi(q_\parallel,0)=1-V(q_\parallel)\Pi_1(q_\parallel,0)$ is the screening factor [see Eqs. (39) and (70)–(75) in Ref. 16]. $\xi(q_\parallel,0)$ makes interband matrix element $\tilde{M}^{\rm II}_{s',s}(\mathbf{q}_\parallel)$ be the short range, i.e., it is finite at $q_\parallel=0$. In the calculations we set $C_{\rm II}\equiv I_{s',s}(q_\parallel)I_{\rm cc}I_{\rm cv}$ in Eq. (8) as the only adjustable parameter in the following calculations, which is determined by fitting to experiments.

The total energy-gain rate is defined by

$$S=S_{\rm i}+S_{\rm p}+S_{\rm II}. \tag{9}$$

The combination of both n and $-n$ terms in Eqs. (5)–(7) represents the total net contribution to S from the n-photon ($n\geqslant1$) emission and absorption processes. We therefore write S in a sum of all orders of n-photon contributions,

$$S=\sum_{n=1}^{\infty}S_n, \tag{10}$$

where S_n is the total contribution from terms having index n and $-n$ in Eqs. (5)–(7). For quasi-2D systems, we can use the ratio of the energy loss of the electromagnetic radiation after passing through the 2D sheet to the energy of the electromagnetic wave into the system, as a measure of the absorption of the radiation. By a direct manipulation, we obtain the nonlinear free-carrier absorption percentage,

$$\alpha=\frac{2S}{\sqrt{\kappa}\varepsilon_0cE^2_{\rm ac}}, \tag{11}$$

in which c is the light speed in vacuum. To see the role of individual multiphoton processes, we define

$$\alpha_n=\frac{2S_n}{\sqrt{\kappa}\varepsilon_0cE^2_{\rm ac}} \tag{12}$$

to be the contribution of the *n*-photon (absorption and emission) process to the total absorption percentage, $\alpha=\Sigma_{n=1}^{\infty}\alpha_n$.

III. ABSORPTION OF THz RADIATIONS IN InAs/AlSb HETEROJUNCTIONS

Applying Eqs. (2)–(4), we have performed numerical calculations for transport properties in THz-driven InAs/AlSb HJ's. We consider the electron-acoustic-phonon scattering (via the deformation potential and the piezoelectric couplings), electron-polar-optical-phonon scattering (via the Fröhlich coupling), and elastic scattering both from the remote charged impurities and from the background impurities. Kane-type nonparabolic dispersion is used in calculating the inverse effective mass tensor $\mathcal{K}$ in Eq. (2). The nonparabolic factor is set to be $\alpha=2.73\ \mathrm{eV}^{-1}$ for InAs. The role of the three lowest subbands ($s=0$, 1, and 2) is taken into account. The band-gap energy is $E_g=0.22$ eV. The energies of the electron subbands are set to be $\varepsilon_0=0$, $\varepsilon_1=35$ meV, and $\varepsilon_2=200$ meV. Up to ten hole subbands are taken into account. We set the sheet density of InAs well $N_0=5\times10^{12}\ \mathrm{cm}^{-2}$, depletion layer charge density $N_{\mathrm{dep}}=5\times10^{10}\ \mathrm{cm}^{-2}$, background impurity $n_{\mathrm{I}}=6.86\times10^{15}\ \mathrm{cm}^{-3}$, and remote impurities in AlSb barrier $N_{\mathrm{I}}=1.53\times10^{11}\ \mathrm{cm}^{-2}$ located at a distance of $l=10$ nm from the interface of the HJ. In the whole paper, the lattice temperature is set to be $T=300$ K, and the dc field is assumed to be $E_0=1.5$ V/m, same as that used in the experiments.[5] The only adjustable parameter C_{II} appearing in Eq. (8) is taken to be $C_{\mathrm{II}}=0.114$ throughout the calculations. We have included contributions from as many optical channels as needed for reaching a required integral accuracy of 10^{-4}, i.e., the orders of the Bessel functions *n* in Eqs. (5)–(7) are set to be large enough so that the integrals are convergent within the accuracy. The maximum of multiple photon orders have been self-consistently determined by the computing program. The material parameters used here are typical values for InAs/AlSb HJ's.

When a dc electric field E_0 and an intense THz field in the form of Eq. (1), $E(t)=E_0+E_{\mathrm{ac}}\sin(2\pi f_{\mathrm{ac}}t)$, are applied to the direction parallel to the interface of InAs/AlSb HJ, the II process is treated as a kind of scattering mechanism, and is included by accounting for the II-induced frictional acceleration $A_{\|}$, II-induced energy-loss rate $W_{\|}$, II-induced energy-gain rate $S_{\|}$, and the electron-hole generation rate *g*. When the radiation is intense enough II processes occur and contribute to carrier transport. In Figs. 1(a)–(d) we have respectively shown the calculated electron velocity $v(t)$, electron temperature $T_e(t)$, sheet density $N(t)$, and the net carrier generation rate $g(t)$ as functions of time for the radiation field with $E_{\mathrm{ac}}=5$ kV/cm and $f_{\mathrm{ac}}=1$ THz at lattice temperature $T=300$ K. The corresponding locally enlarged figures in the initial 60 ps are respectively plotted as their insets. During the time evolution of the transport state there are two noticeable steady states. One is the quasisteady state (QSS), as indicated by the insets, and the another is the complete steady state (SS), as shown in Figs. 1(a)–(d). In the QSS case, carrier velocity and electron temperature almost become steady, i.e., they look like being independent of time

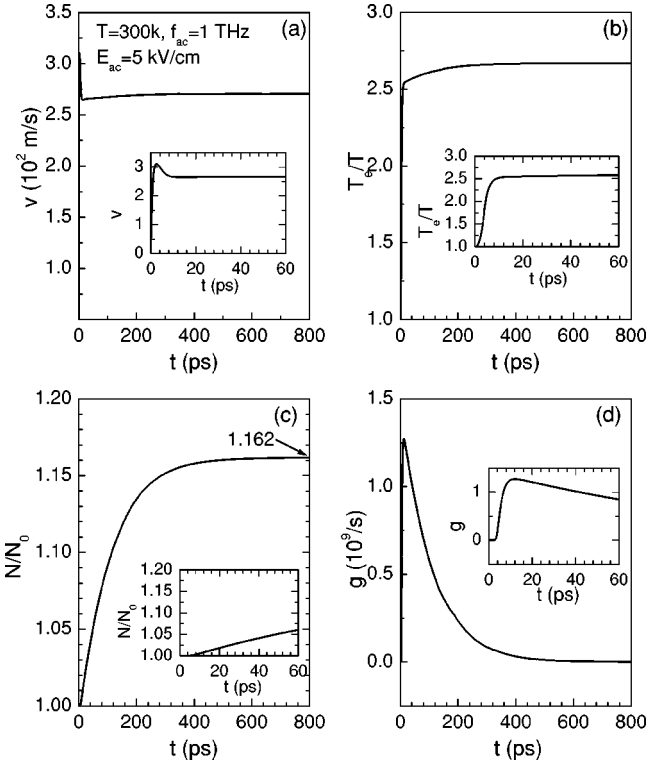

FIG. 1. (a) Calculated electron drift velocity $v(t)$, (b) electron temperature $T_e(t)$, (c) electron number $N(t)$, and (d) electron-hole generation rate $g(t)$ as functions of time in InAs/AlSb heterojunction (HJ) driven by the THz radiation with $E_{\mathrm{ac}}=5$ kV/cm and $f_{\mathrm{ac}}=1$ THz at lattice temperature $T=300$ K. The corresponding locally enlarged figures in the initial 60 ps are respectively plotted as their insets.

evolution [see the insets of Figs. 1(a) and (b)], while the total number of carriers is still increasing due to the II process with a net electron-hole generation rate $g(=dN/dt)$ [see the inset of Fig. 1(c)]. The total number of carriers *N* in the QSS case is, however, not too far from the initial carrier number N_0. With the further evolution of time the QSS breaks up. The number of carriers increases more and more up to the complete SS with $N/N_0=1.162$ [see Fig. 1(c)]. The electron velocity and electron temperature also increase with the time evolution, and finally approach their SS at about $t>800$ ps. At the complete SS case, electron-hole generation rate and recombination rate are equal, leading a zero net generation rate ($g=0$), as shown in Fig. 1(d). In the SS case, all the transport qualities are constants, hence they can be directly solved from Eqs. (2)–(4) by setting the right-hand sides to be zero ($d\mathbf{v}/dt=0$, $dh_e/dt=0$, and $dN/dt=0$). In Fig. 2 we show the calculated electron number N/N_0 and (b) electron temperature T_e/T as functions of wavelength λ of THz radiations at different THz radiation strengths $E_{\mathrm{ac}}=4.5$, 5, 5.8, 7, and 9 kV/cm, respectively. The electron number N/N_0 and electron temperature T_e/T monotonically increases with increasing the radiation strength E_{ac} and/or increasing the wavelength λ. For each E_{ac} the carrier number and the electron temperature increases with the frequency f_{ac}. It can be seen that larger radiation strength and lower radiation fre-

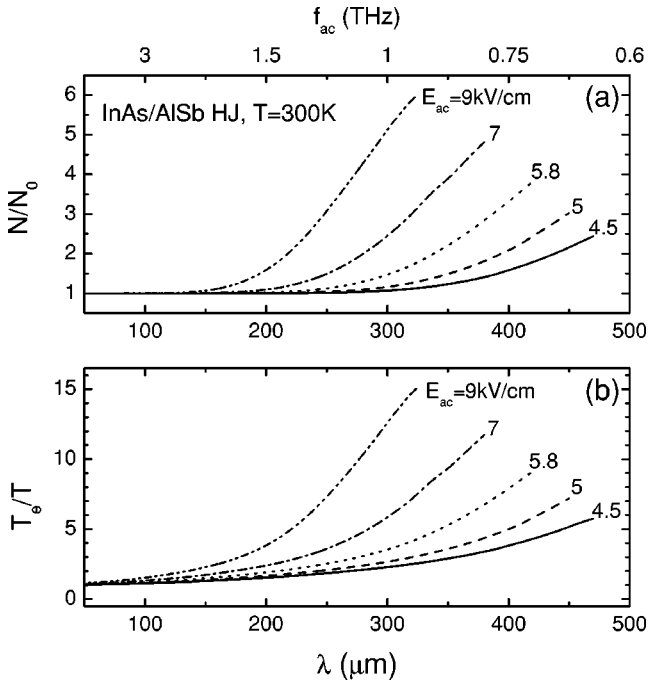

FIG. 2. (a) Calculated electron number N/N_0 and (b) electron temperature T_e/T as functions of wavelength λ of THz radiations in InAs/AlSb heterojunctions at different THz radiation strengths E_{ac} = 4.5, 5, 5.8, 7, and 9 kV/cm, respectively. In the whole paper, the lattice temperature is T = 300 K.

quency lead to a larger electron-hole generation and higher electron temperature. Actually, the role of THz radiation field on carrier transport increases with increasing the factor $r_\omega = eE_{ac}/(m\omega^2)$, appearing in the Bessel function in Eqs. (5)–(7).

In Fig. 3 we show absorption percentage α of THz radiations in the InAs/AlSb HJ as functions of the amplitudes E_{ac} at different radiation frequencies f_{ac} = 0.64, 0.8, and 1 THz, respectively. The solid circles are the experimental results for f_{ac} = 0.64 THz from Ref. 5, where $\alpha = 1 - T - R$ with T the transmission and R the reflection. Good agreement is obtained between the calculated results and the experimental data. It is seen from Fig. 3 that, lower frequency leads to

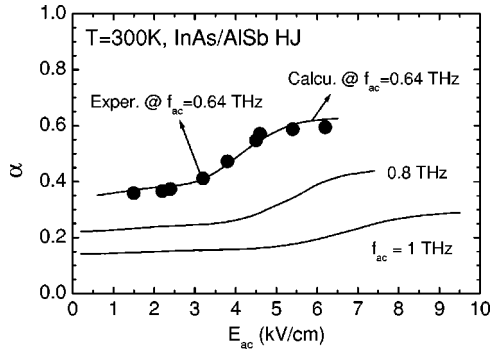

FIG. 3. Absorption percentage α of THz radiations in InAs/AlSb heterojunctions as functions of the amplitudes E_{ac} at different radiation frequencies f_{ac} = 0.64, 0.8, and 1 THz, respectively. The solid circles are the experimental results from Ref. 5.

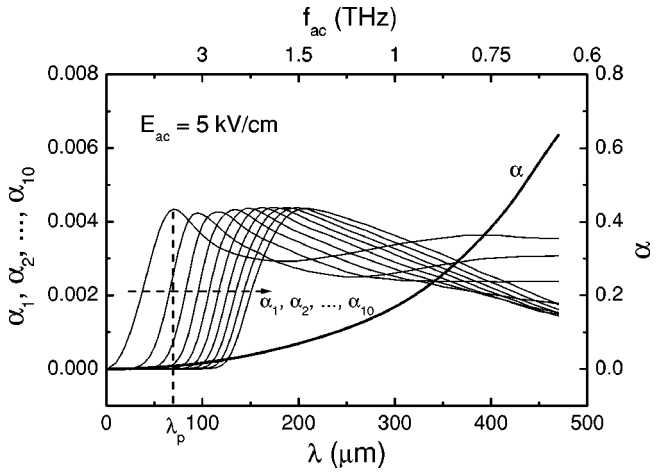

FIG. 4. The n-photon contribution α_n (n = 1,2,3,...,10) and the total absorption percentage α (light axis) versus the wavelength λ of THz radiation at a fixed amplitude E_{ac} = 5 kV/cm.

more absorption of THz radiations. The absorption rate increases slowly from low electric field to 3 kV/cm, then goes fast before reaching its saturation value. To see the role of individual multiphoton processes we have shown in Fig. 4 the first ten order photon contribution α_n (n = 1,2,3,...,10) and the total absorption percentage α (light axis) versus the wavelength λ (or the frequency f_{ac}) at a fixed amplitude E_{ac} = 5 kV/cm. For each order of multiphoton channels there is a critical wavelength λ_p at which the multiphoton process makes maximal contribution to the total absorption. With increasing the order the position of λ_p shifts to longer wavelength. The physical origin of the critical wavelength at a given photon number is that, for a given n, the strength of the scattering matrix of the n-photon assisted process (showing up mainly in the Bessel function J_n^2) decreases almost like ω^{-4n} for large ω, while the energy absorpted from the radiation field during each n-photon process is proportional to $n\omega$. There must be a critical wavelength λ_p at which the energy absorption reaches a maximum, and the position of λ_p shifts towards the direction of longer wavelength with increasing n. This is the reason for the critical wavelength at a given photon number n, as shown in Fig. 4. However, it is accidental for the present system and the applied THz field that all the maxima in Fig. 4 have approximately the same height. In Fig. 5 we have shown the n-photon contribution α_n (n = 1,2,3,...,10) and the total absorption percentage α (light axis) versus the amplitude E_{ac} at given frequency f_{ac} = 1 THz. It is seen that although the single-photon process dominates for $E_{ac} < 0.4$ kV/cm, its contribution decreases quickly with increasing E_{ac}, and multiphoton ($n \geqslant 2$) processes play more important role on the absorption. The inset of Fig. 5 shows the maximal orders of the multiple-photon channels, n_{ei}, n_{eph}, and n_{II}, respectively related to electron-impurity scattering, electron-phonon scattering, and II process, as functions of the amplitude E_{ac}. They are self-consistently yielded by the computing program in doing the summation over n in Eqs. (5)–(7) within the integral accuracy of 10^{-4}. It is indicated that the order of II-related multiple-photon channels, n_{II}, is usually larger than those

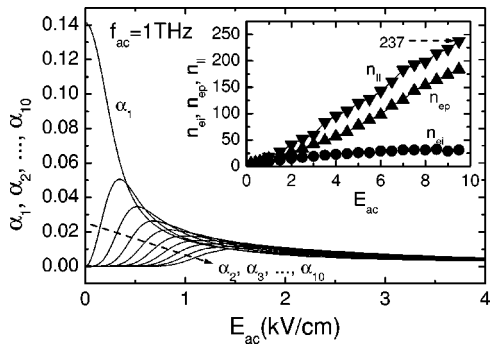

FIG. 5. The n-photon contribution α_n ($n=1,2,3,...,10$) and the total absorption percentage α (light axis) versus the amplitude E_ω of the radiation field at a fixed frequency $f_{ac}=1$ THz. The inset shows the orders of the multiple-photon channels, n_{ei}, n_{eph}, and n_{II}, respectively related to electron-impurity scattering, electron-phonon scattering, and II process, as functions of the amplitude E_ω of the radiation field. They are self-consistently yielded by the computing program.

related to electron-impurity scattering (n_{ei}) and electron-phonon scattering (n_{eph}), and more multiple-photon channels are needed to be taken into account for larger radiation strength and lower radiation frequency. When $E_{ac}=9.5$ kV/cm even the n-photon channels with n as large as 237 are not negligible in order to get the accuracy of 10^{-4} (see the inset of Fig. 5). For given ω, the maximal orders of the multiphoton channels needed to reach the given numerical accuracy of 10^{-4} is judged by magnitude of their contributions to A, W, S, and g. For each mechanism this is determined, in addition to the strength coefficient of the individual scattering process, by (i) the q dependence of the bare scattering matrix elements and (ii) the energy exchange during the scattering process. The matrix elements for electron-LO phonon scattering and for impact ionization process have a similar q dependence and the energy exchange difference between $E_g+n\omega$ and $\Omega_{LO}+n\omega$ is not so great for n as large as 200. This is the physical reason why the difference of the maximal orders needed for impact ionization and for LO-phonon scattering is not very big.

IV. CONCLUSIONS

In conclusion, by considering multiple photon process and conduction-valence interband impact ionization, we have studied the impact ionization effect and the free-carrier absorption rates of intense terahertz (THz) radiation in InAs/AlSb heterojunctions (HJ's). We have considered the electron-acoustic-phonon scattering (via the deformation potential and the piezoelectric couplings), electron-polar-optical-phonon scattering (via the Fröhlich coupling), and elastic scattering both from the remote charged impurities and from the background impurities. As many as needed multiphoton channels are taken into account for yielding a required accuracy. It is indicated that, the role of THz radiation field on the absorption and II process increases with increasing the THz radiation strength or decreasing the THz radiation frequency. Multiple-photon processes are investigated in details. Absorption percentages for InAs/AlSb HJ's at $f_{ac}=0.64$ THz are reasonably reproduced by the present calculations, and qualitatively compared to available experiments.

ACKNOWLEDGMENTS

This work was supported by the National Natural Science Foundation of China, the Special Funds for Major State Basic Research Project (2001CCA02800G and 20000683), and the Special Funds for Shanghai Optic Engineering (011661075).

[1] N. G. Asmar, A. G. Markelz, E. G. Gwinn, J. Cerne, M. S. Sherwin, K. L. Campman, P. F. Hopkins, and A. C. Gossard, Phys. Rev. B **51**, 18 041 (1995).
[2] B. J. Keay, S. J. Allen, Jr., J. Galán, J. P. Kaminski, K. L. Campman, A. C. Gossard, U. Bhattacharya, and M. J. W. Rodwell, Phys. Rev. Lett. **75**, 4098 (1995).
[3] B. J. Keay, S. Zeuner, S. J. Allen, Jr., K. D. Maranowski, A. C. Gossard, U. Bhattacharya, and M. J. W. Rodwell, Phys. Rev. Lett. **75**, 4102 (1995).
[4] K. Unterrainer, B. J. Keay, M. C. Wanke, S. J. Allen, D. Leonard, G. Medeiros-Ribeiro, U. Bhattacharya, and M. J. W. Rodwell, Phys. Rev. Lett. **76**, 2973 (1996).
[5] A. G. Markelz, N. G. Asmar, B. Brar, and E. G. Gwinn, Appl. Phys. Lett. **69**, 3975 (1996).
[6] X. L. Lei, J. Appl. Phys. **84**, 1396 (1998).
[7] X. L. Lei, J. Phys.: Condens. Matter **10**, 3201 (1998).
[8] X. L. Lei and H. L. Cui, Eur. Phys. J. B **4**, 513 (1998).
[9] J. C. Cao, H. C. Liu, and X. L. Lei, J. Appl. Phys. **87**, 2867 (2000).
[10] J. C. Cao, H. C. Liu, X. L. Lei, and A. G. U. Perera, Phys. Rev. B **63**, 115308 (2001).
[11] J. C. Cao, X. L. Lei, A. Z. Li, and H. C. Liu, Appl. Phys. Lett. **78**, 2524 (2001).
[12] J. C. Cao, A. Z. Li, X. L. Lei, and S. L. Feng, Appl. Phys. Lett. **79**, 3524 (2001).
[13] X. F. Wang, I. C. da Cunha Lima, X. L. Lei, and A. Troper, Phys. Rev. B **58**, 3529 (1998).
[14] J. C. Cao and X. L. Lei, Eur. Phys. J. B **7**, 79 (1999).
[15] X. L. Lei, N. J. M. Horing, and H. L. Cui, Phys. Rev. Lett. **66**, 3277 (1991).
[16] X. L. Lei, J. L. Birman, and C. S. Ting, J. Appl. Phys. **58**, 2270 (1985).
[17] T. Ando, A. B. Fowler, and F. Stern, Rev. Mod. Phys. **54**, 437 (1982).